ChemComm

Nanoscale Kinetic Imaging of Lithium Ion Secondary Battery Materials using Scanning Electrochemical Cell Microscopy

Journal:	*ChemComm*
Manuscript ID	CC-COM-04-2020-002865.R1
Article Type:	Communication

ChemComm

COMMUNICATION

Nanoscale Kinetic Imaging of Lithium Ion Secondary Battery Materials using Scanning Electrochemical Cell Microscopy

Received 00th January 20xx,
Accepted 00th January 20xx

DOI: 10.1039/x0xx00000x

www.rsc.org/

Yasufumi Takahashi[a,b*], Tsubasa Yamashita[a], Daiko Takamatsu[c*], Akichika Kumatani[d], Takeshi Fukuma[a]

To visualize the electrochemical reactivity and diffusion coefficient of the anode of lithium-ion batteries, we placed scanning electrochemical cell microscopy (SECCM) in a glovebox. The SECCM visualized the facet-dependent diffusion coefficient on an $Li_4Ti_5O_{12}$(LTO) thin-film electrodes and detect the metastable crystal phase of Li_xFePO_4.

Lithium-ion batteries (LIBs) are used in various applications including power sources for mobile devices and electric vehicles owing to their high energy/power density and long cycle life.[1] The nanoscale characteristics of LIBs help to understand the intrinsic performance of active material and structural inhomogeneous reactivity.[2] Time-resolved X-ray diffraction is a useful tool to analyze the phase transition dynamics of LIB's active materials. Orikasa et al. have identified the metastable crystal phase of $LiFePO_4$ (LFP).[3] *In situ* surface-sensitive X-ray absorption spectroscopy has shown that Co reduction at the $LiCoO_2$(LCO) surface resulting from electrolyte contact caused initial degradation.[4, 5] Scanning transmission X-ray microscopy was developed to probe the spatiotemporal evolution of Li composition and insertion rate within primary particles.[6] Electron beam irradiation and electron energy-loss spectroscopy were used to produce and conform Li-insertion reaction at the local region.[7] Near-field optical technique was used to visualize the lithium-ion distribution in a LIB's cathode on a nanometer scale.[8] However, it is difficult to characterize the reaction with spatial and temporal resolution simultaneously.

Ultramicroelectrode (UME) is an effective tool to distinguish the bottleneck process during charging/discharging and to estimate the kinetic parameter of LIBs.[9] Dokko et al. have developed a single-particle measurement approach, which uses a microelectrode for the evaluation of the intrinsic performance of primary or secondary single active material by directly attaching UME to the particle. [10-13] Compton et al. have fabricated $LiMn_2O_4$ single particle-coated UME and evaluated the rate-determining step.[14] UME that is in contact with single particles provides an ideal electron pass and ion access owing to the formation of the sphere shape diffusion layer. However, the single-particle measurement using UME does not have a spatial resolution, and the electrochemical signal was averaged at the single crystal level. Therefore, facet level electrochemical characterization was difficult to achieve using this technique.

Scanning electrochemical microscopy (SECM), which uses UME as a probe, is a powerful tool for characterizing the surface reactivity and electrochemical properties of the sample with spatial resolution.[15-20] For battery materials, the SECM feedback mode is effective for monitoring the solid-electrolyte interface formation.[21-24] For the direct quantitative investigation of spatially resolved ionic processes, mercury-capped platinum ultramicroelectrodes have been developed and used for Li^+ imaging that is based on Li stripping.[25] Scanning gel electrochemical microscopy (SGECM) was also reported to perform local electrochemical measurements using a gel probe.[26, 27] SGECM can control electrochemical cell size by the applied vertical pressure to the gel probe and has a possibility to avoid evaporation of electrolyte solution during long-time measurement. Scanning electrochemical cell microscopy (SECCM), which uses a nanopipette as a probe and forms a local electrochemical cell, is an effective tool for characterizing surface reactivity. [28-31] SECCM has been applied to the electrochemical imaging of a LIB's cathode material at the sub-micrometer resolution.[31-35] This approach allows to determine local electrochemical properties by scanning the nanopipette. The advantages of SECCM for battery material research are its high spatial resolution, small capacitive current, and isolated electrochemical cell. However, conventional SECCM is used under atmospheric conditions.

In this study, we placed SECCM in a glovebox to perform analysis in a well-defined argon gas atmosphere to study the kinetic parameter of polycrystalline LCO and LTO thin-film electrodes and single LFP particles. We compared the cyclic voltammetry (CV) of LCO and LTO, evaluated the diffusion coefficient, and mapping the diffusion coefficient on the LTO surface using SECCM. The metastable crystal phase of Li_xFePO_4 was also detected using the nanoscale electrochemical cell of SECCM.

Owing to the electrochemical potential window and reference electrode issues for characterizing the anode of LIB's, we placed SECCM in an argon-filled glove box (Fig. S1). To remove vibrations from the SECCM system, we placed an antivibration table into the glovebox. SECCM measurement was carried out in a dry argon-filled glovebox wherein the atmosphere contained low levels of oxygen (~1.0 ppm) and water (dew point lower than −70°C). During SECCM imaging, we shut off the pumps to avoid the vibration.

[a] *Nano Life Science Institute (WPI-NanoLSI), Kanazawa University, Kakuma-machi, Kanazawa 920-1192, Japan*
[b] *Precursory Research for Embryonic Science and Technology (PRESTO), Japan Science and Technology Agency (JST), Saitama 332-0012, Japan*
[c] *Center for Exploratory Research, Research & Development Group, Hitachi, Ltd., Hatoyama-machi, Saitama 350-0395, Japan*
[d] *WPI-Advanced Institute for Materials Research (AIMR), Tohoku University, 2-1-1-509, Katahira, Aoba-ku, Sendai 980-8577, Japan*

†*Electronic Supplementary Information (ESI) available: See DOI: 10.1039/x0xx00000x*

The structural and electrochemical characterization of LCO thin films prepared by the PLD techniques has been described in the previous paper.[36] Figure 1 summarizes the structural and electrochemical properties of the LTO thin-film electrode prepared by PLD on flat Pt/Cr/Si substrates. Figure 1(a) shows the typical out-of-plane XRD pattern of LTO thin films. The pattern matched the Fd-3 m spinel structure (ICDD card no: 049-0207) as well as a small amount of TiO_2 impurity and peaks that originated from the substrate. Figure 1(b) shows constant-current (1/2C rate) charging/discharging curves of 1st and 2nd cycles between 1 V and 2.5 V *vs.* Li/Li^+. The flat redox potential at 1.55 V is clearly indicative of the two-phase reaction between $Li_4Ti_5O_{12}$ and $Li_7Ti_5O_{12}$.[37] It is known that the charge (delithiation) and discharge (lithiation) reactions of LTO are difficult to characterize by XRD owing to the zero-strain transition between $Li_7Ti_5O_{12}$ and $Li_4Ti_5O_{12}$.[38] However, the most significant property difference between the two phases is electronic conductivity (i.e., $Li_7Ti_5O_{12}$ is electronically conductive, while $Li_4Ti_5O_{12}$ is an insulator).[39] Figure 1(c) shows the topography and current images of LTO electrodes, which were disassembled and dried at points A–C of (b). Conductive atomic force microscopy (c-AFM) was performed by applying the potential of 0.5 V between the c-AFM tip and the substrate. Topography images show that triangle-like structures can be observed on LTO thin films. The previous report has characterized the triangle-like structures as LTO (111) crystal facets.[40] Figure 1(d) shows the STEM cross-section image of LTO thin film electrode. STEM image revealed the complex nanostructure of this film. It is assigned a well-crystallized phase on the center of the image to LTO (111) crystal. c-AFM current images showed that the number of conductive grains considerably increased with lithiation (from A to C), while the surface morphology did not considerably change by the state of charge (SOC). This result is consistent with the reported c-AFM measurements.[41] Of note, thin films used in this study have a polycrystalline structure, which is suitable to simulate the conditions of applied composite electrodes.

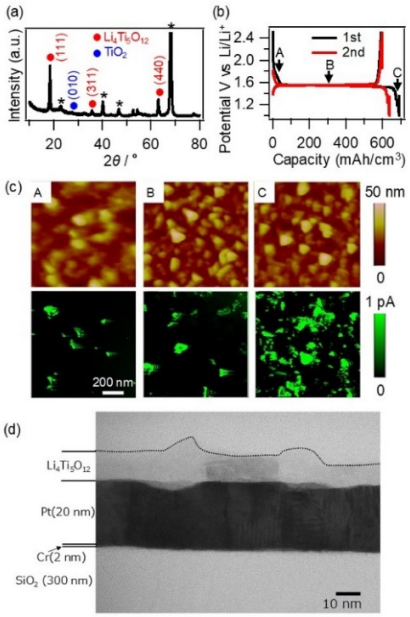

Figure 1. (a) Out-of-plane XRD spectra of the LTO thin film on the Pt/Cr/Si substrate. *: Peaks originated from the substrate (Pt, Pt3Ti). (b) Constant-current (1/2C rate) charging and discharging curves of the cell com-posed of the LTO thin-film electrode as WE and Li metal as CE/RE. (c) Ex situ c-AFM images of LTO thin-film electrodes that were disassembled and dried at the points A–C of (b). (Upper) Topography and (Bottom) current images. Scan size: 1 × 1 μm², Vs = 0.5 V. (d) Cross-sectional STEM image of LTO thin film on the Pt/Cr/Si substrate.

The nanoscale electrochemical cell formed by the SECCM nanopipette can diminish capacitive current and provides fast electrochemical measurements without IR drop at the end of the nanopipette because of the small current.[32, 42] To characterize the reactivity of LTO and LCO (i.e., reaction progress with two-phase and solid solution reactions), we performed fast scan rate CV using SECCM with 55 nm radius nanopipette (Fig.2(a,b)). Li^+ (de)intercalation chemistry at $LiCoO_2$ and $Li_7Ti_5O_{12}$ can be expressed by Eq. (1) and (2), respectively.

$$LiCoO_2 \rightleftharpoons Li_{1-x}CoO_2 + xLi + xe^- \quad (0 \le x \le 0.55) \quad (1)$$

$$Li_7Ti_5O_{12} \rightleftharpoons Li_4Ti_5O_{12} + 3Li + 3e^- \quad (2)$$

The peak redox potential of LTO and LCO obtained by SECCM corresponded to that in the previous report.[37, 43] LTO shows small peak separation and sharp oxidation and reduction current is clearly observed even at 500 mV/s. The LTO and LCO peak separations at the CV scan rates of 10 mV/s, 100 mV/s and 500 mV/s were 57 mV, 74 mV, 136 mV and 155 mV, 426 mV, 736 mV, respectively. In the case of LCO experiment, wide peak separation and broad peak current were observed. The peak current was not observed when the scan rates were over 100 mV/s. These CV response differences were observed by SECCM fast scan CV derived from the diffusion coefficient differences. The reduction peak current is smaller than that of the oxidation current. This is attributed to the difference in conductivity. This phenomenon was confirmed by the single-crystal experiment.[44] The SECCM nanoscale electrochemical measurement can distinguish the reactivity difference of LTO and LCO within a few tens of seconds (500 mV/s).

The diffusion coefficient evaluation is also a suitable application of SECCM. The diffusion coefficients of polycrystalline LTO and LCO thin-film electrodes have been reported to be 10^{-9}–10^{-16} $cm^2 \cdot s^{-1}$ and 10^{-11}–10^{-13} cm^2/s, respectively.[40, 45] Diffusion coefficients considerably vary depending on the characterization technique used. Therefore, it is important to characterize the diffusion coefficient using a simple and reliable method. The peak current of CV depends on the scan rate.[46] The Randles−Sevcik equation (3) is used to estimate the diffusion coefficient.

$$i_p = 0.4463nFAC\left(\frac{nF\upsilon D}{RT}\right)^{\frac{1}{2}} \quad (3)$$

The peak current i_p (A) increases linearly with the square root of the scan rate υ (Vs^{-1}), where n is the number of electrons transferred in the redox event, A (cm^2) is the sample surface area, D (cm^2s^{-1}) is the diffusion coefficient of the electrolyte, and C (mol cm^{-3}) is the bulk concentration of the electrolyte. Denis and coworkers evaluated Li^+ diffusion coefficient within the LFP composite electrode using Randles-Sevcik equation.[47] To estimate the diffusion coefficient within the active materials using Randles-Sevicik equation, Li^+ diffusion state in solution is faster enough than the diffusion state within active materials. The micro/nano-scale electrochemical measurement provides a high mass transfer characterization because of the semi-sphere Li^+ diffusion state.[10-12] This is an ideal situation for evaluating the Li^+ diffusion coefficient within the active material.

When the CV scan rate is considerably slower compared to the diffusion of Li within the active material, the peak current is proposed to be the square root of the scan rate. We recorded CVs at different scan rates (i.e., 0.1–200 mV/s) using 55 nm radius nanopipette and plotted the graphs of peak current vs. the square root of the scan rate (Fig.2 (c)). If the CV scan rate speed is higher than the speed of

Li diffusion within the active material, the response cannot be fit with the square root of the scan rate. In the case of LTO, the maximum sweep rate of CV that can fit the peak current linearly was found to be 25 V/s. The LTO diffusion coefficient evaluated using the Randles–Sevcik equation was 2.47×10^{-11} (cm^2/s), which agrees with that in the previous report.[48] The detail of the diffusion coefficient calculation was described in supporting information.

The charging/discharging characteristics are also important for the evaluation of battery material performance. However, for the organic solution measurement of SECCM, the meniscus state is not stable compared to that of aqueous solution[32] owing to the evaporation problem of the organic solution. For this reason, we used a micropipette (5.0 μm radius) for this charge/discharge experiment to form a stable meniscus on the LTO surface to evaluate charging/discharging characteristics. Using the 5.0 μm radius pipette, we were able to monitor the charge/discharge characteristics for 1600 s (Fig.2(d)). For the fast discharging process, discharge capacity was smaller than the charging capacity. The difference was related to the conductance difference of LTO. The SECCM local electrochemical characterization allows to determine material properties (e.g., conductance-dependent capacity difference) without using a single crystal.

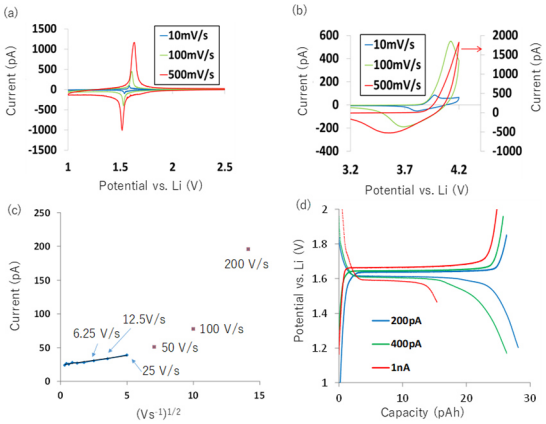

Figure 2. Cyclic voltammetry on (a) LTO and (b) LCO thin-film electrodes. Li metal was used as a reference electrode. (c) Relationship of the CV peak current to $(Vs^{-1})^{1/2}$ on LTO. (d) Charging/discharging characteristics on LTO. Nanopipette filled with 1.0 M $LiClO_4$ in EC:DEC (1:1 v/v%). The nanopipette radii were (a-c) 55 nm and (d) 5.0 μm, respectively.

To visualize the reactivity inhomogeneity derived from the facet difference of the LTO thin-film electrode, SECCM Li^+ deintercalation current imaging was performed. In this experiment, we used 55 nm radius nanopipette and applied 1.3 V *vs.* Li/Li^+ to detect Li^+ deintercalation currents. SECCM current images are shown in Figure 3(a). SECCM allowed to visualize inhomogeneous low current response region, which sizes are 300–500 nm. The different current response was derived from the crystal facet difference, which agreed with the c-AFM analysis shown in Fig 1(c). SECCM can be also used to evaluate the diffusion coefficient at each imaging pixel to map the inhomogeneity of the diffusion coefficient on the sample surface. We developed the diffusion coefficient mapping program, which performs different scan rate CV (1.25, 2.5, 5.0, 10, 20 V/s) measurements at each imaging pixels to evaluate the diffusion coefficient by fitting the peak current and the square root of the scan rate [Fig. 3(c)]. Figure 3(b) shows the image of the diffusion coefficient mapping on the polycrystalline LTO thin-film electrode by SECCM. The polycrystalline facet-dependent inhomogeneous diffusion coefficient was visualized and evaluated by SECCM as a 2D image. The response region is similar to that of the current image in Fig. 3(a).

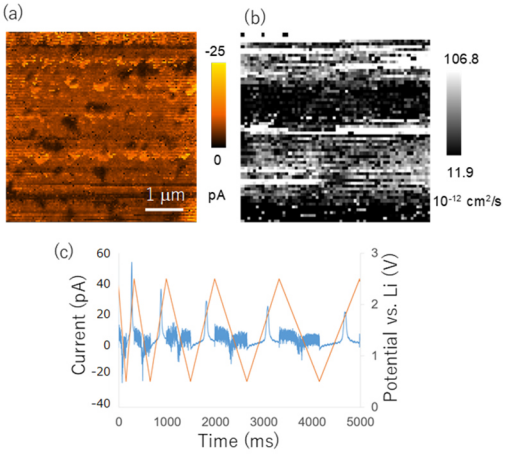

Figure 3. SECCM (a) current and (b) diffusion coefficient images of the LTO thin-film electrode. Li metal used as a reference electrode. Nanopipette filled with 1.0 M $LiClO_4$ in EC:DEC(1:1v/v%) was utilized. Scan size: 5 × 5 μm^2. (a) The image was acquired by applying the constant voltage of 1.3 V *vs.* Li/Li^+. Pixel number: 128 × 128. (b) Pixel number: 64 × 64. (c) Typical cyclic voltammetry response with a different sweep rate on the LTO thin-film electrode. Sweep rate: 20, 10, 5, 2.5, and 1.25 V/s. (b) Diffusion coefficient mapping on the LTO thin-film electrode. Nanopipette radius was 55 nm.

Then, we characterize the LFP secondary single particle. Although we have already examined SECCM on LFP using an aqueous electrolyte with an Ag/AgCl reference, this is the first attempt of using an organic electrolyte with a Li/Li^+ reference. Li^+ (de)intercalation chemistry at $LiFePO_4$ can be expressed by Eq. (4).

$$LiFePO_4 \rightleftharpoons FePO_4 + Li + e^- \quad (4)$$

LFP single particles were dispersed on the Au substrate and pressed tightly to be immobilized on the substrate. The SECCM topography and current images of LFP particles are shown in Figure 4(a, b). In this experiment, we used 55 nm radius nanopipette. The current response can be obtained for LFP particles. Then, we performed CV at different scan rates (1–1000 mV/s). LFP is known as the active material that is capable of fast charging/discharging. Actually, we can clearly observe oxidation and reduction current even at 1000 mV/s. When the scan rate of CV was slow (e.g., less than 10 mV/s), we could observe double peak oxidation and reduction current. The current response at approximately 3.4 V *vs.* Li/Li^+ seems to be derived from the metastable state of Li_xFePO_4 (Fig. 4(c, d)). The lifetime of the metastable phase depends on the charge/discharge rate or the CV scan rate. Similarly, Orikasa et al. observed the metastable state of LFP charging/discharging at 10 C using *in situ* XAFS/XRD measurements.[3] The CV scan rate of 10 mV/s corresponds to ca. 25 C in this experiment. Thanks to the relatively high-speed CV of the SECCM compared to the conventional electrochemical measurement, we can observe the metastable state-related current as the CV current response. These results indicated that SECCM will become a versatile tool for the evaluation of the kinetic character of LIBs electrodes.

In this study, we developed SECCM that was placed in a glovebox, and the kinetic behavior difference of polycrystalline LTO and LCO thin-film electrodes was characterized. Diffusion coefficient mapping was also performed by SECCM. The SECCM

current and diffusion coefficient images visualized the inhomogeneous current response distribution on the LTO thin-film electrode. Owing to the fast and highly sensitive electrochemical characterization of SECCM, the metastable state of LFP could be observed. The developed system allows to visualize the diffusion coefficient difference at grain boundaries and crystal facets and to characterize the metastable state, which cannot be evaluated by conventional electrochemical measurements.

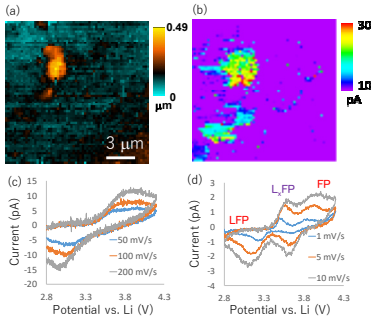

Figure 4. SECCM (a) topography and (b) current images of the secondary single LFP particle. Li metal used as a reference electrode. Nanopipette filled with 1.0 M $LiClO_4$ in EC:DEC (1:1 v/v%). Scan size: 15 × 15 μm^2. The image was acquired by applying the constant voltage of 4.2 V *vs.* Li/Li^+. Pixel number: 128 × 128. (c, d) Cyclic voltammetry with a different sweep rate on the secondary single LFP particle. Nanopipette radius was 55 nm.

The authors acknowledge support for this work from PRESTO (JPMJPR18T8) from the Japan Science and Technology Agency (JST), a Grant-in-Aid for Scientific Research (A) (19H00915), a Grant-in-Aid for Young Scientists (A) (15H05422 and 16H06042), a Grant-in-Aid for Exploratory Research (15K13263 and 17K19135), Grant-in-Aid for Scientific Research on Innovative Areas (16H00885), and Grant-in-Aid for Scientific Research on Innovative Areas "Interface IONICS" (19H05814) from the Japan Society for the Promotion of Science (JSPS), World Premier International Research Center Initiative (WPI), MEXT, Japan and Asahi Glass Foundation, Grant-in-Aid for Young Scientists provided by Hokuriku bank, Murata Science Foundation, and Intelligent Cosmos Academic Foundation.

Conflicts of interest

There are no conflicts to declare.

References

1. M. Armand and J. M. Tarascon, *Nature*, 2008, **451**, 652-657.
2. S.-K. Jung, I. Hwang, D. Chang, K.-Y. Park, S. J. Kim, W. M. Seong, D. Eum, J. Park, B. Kim, J. Kim, J. H. Heo and K. Kang, *Chem Rev*, 2019.
3. Y. Orikasa, T. Maeda, Y. Koyama, H. Murayama, K. Fukuda, H. Tanida, H. Arai, E. Matsubara, Y. Uchimoto and Z. Ogumi, *J Am Chem Soc*, 2013, **135**, 5497-5500.
4. D. Takamatsu, T. Nakatsutsumi, S. Mori, Y. Orikasa, M. Mogi, H. Yamashige, K. Sato, T. Fujimoto, Y. Takanashi, H. Murayama, M. Oishi, H. Tanida, T. Uruga, H. Arai, Y. Uchimoto and Z. Ogumi, *Journal of Physical Chemistry Letters*, 2011, **2**, 2511-2514.
5. D. Takamatsu, Y. Koyama, Y. Orikasa, S. Mori, T. Nakatsutsumi, T. Hirano, H. Tanida, H. Arai, Y. Uchimoto and Z. Ogumi, *Angewandte Chemie-International Edition*, 2012, **51**, 11597-11601.
6. J. Lim, Y. Y. Li, D. H. Alsem, H. So, S. C. Lee, P. Bai, D. A. Cogswell, X. Z. Liu, N. Jin, Y. S. Yu, N. J. Salmon, D. A. Shapiro, M. Z. Bazant, T. Tyliszczak and W. C. Chueh, *Science*, 2016, **353**, 566-571.
7. M. Kitta and M. Kohyama, *Phys Chem Chem Phys*, 2017, **19**, 11581-11587.
8. K. Hara, T. Yano, J. Hata, K. Hikima, K. Suzuki, M. Hirayama, R. Kanno and M. Hara, *Appl Phys Express*, 2017, **10**.
9. A. J. J. Jebaraj and D. A. Scherson, *Accounts Chem Res*, 2013, **46**, 1192-1205.
10. K. Dokko, Y. Fujita, M. Mohamedi, M. Umeda, I. Uchida and J. R. Selman, *Electrochim Acta*, 2001, **47**, 933-938.
11. K. Dokko, M. Mohamedi, Y. Fujita, T. Itoh, M. Nishizawa, M. Umeda and I. Uchida, *J Electrochem Soc*, 2001, **148**, A422-A426.
12. K. Dokko, M. Mohamedi, M. Umeda and I. Uchida, *J Electrochem Soc*, 2003, **150**, A425-A429.
13. H. Munakata, B. Takemura, T. Saito and K. Kanamura, *J Power Sources*, 2012, **217**, 444-448.
14. G. Zampardi, C. Batchelor-McAuley, E. Katelhon and R. G. Compton, *Angew Chem Int Edit*, 2017, **56**, 641-644.
15. E. Ventosa and W. Schuhmann, *Physical Chemistry Chemical Physics*, 2015, **17**, 28441-28450.
16. D. Polcari, P. Dauphin-Ducharme and J. Mauzeroll, *Chem Rev*, 2016, **116**, 13234-13278.
17. Y. Takahashi, A. Kumatani, H. Shiku and T. Matsue, *Analytical Chemistry*, 2017, **89**, 342-357.
18. L. Danis, S. M. Gateman, C. Kuss, S. B. Schougaard and J. Mauzeroll, *Chemelectrochem*, 2017, **4**, 6-19.
19. C. Kranz, *Analyst*, 2014, **139**, 336-352.
20. P. Schwager, H. Bülter, I. Plettenberg and G. Wittstock, *Energy Technol-Ger*, 2016, **4**, 1472-1485.
21. G. Zampardi, E. Ventosa, F. La Mantia and W. Schuhmann, *Chem Commun*, 2013, **49**, 9347-9349.
22. E. Ventosa, G. Zampardi, C. Flox, F. La Mantia, W. Schuhmann and J. R. Morante, *Chem Commun*, 2015, **51**, 14973-14976.
23. G. Zampardi, F. La Mantia and W. Schuhmann, *Rsc Adv*, 2015, **5**, 31166-31171.
24. J. S. Hui, M. Burgess, J. R. Zhang and J. Rodriguez-Lopez, *Acs Nano*, 2016, **10**, 4248-4257.
25. Z. J. Barton and J. Rodriguez-Lopez, *Anal Chem*, 2014, **86**, 10660-10667.
26. N. Dang, M. Etienne, A. Walcarius and L. Liu, *Electrochem Commun*, 2018, **97**, 64-67.
27. N. Dang, M. Etienne, A. Walcarius and L. Liu, *Anal Chem*, 2020, **92**, 6415-6422.
28. A. G. Guell, A. S. Cuharuc, Y. R. Kim, G. H. Zhang, S. Y. Tan, N. Ebejer and P. R. Unwin, *Acs Nano*, 2015, **9**, 3558-3571.
29. B. D. B. Aaronson, C. H. Chen, H. J. Li, M. T. M. Koper, S. C. S. Lai and P. R. Unwin, *J Am Chem Soc*, 2013, **135**, 3873-3880.
30. A. G. Guell, N. Ebejer, M. E. Snowden, J. V. Macpherson and P. R. Unwin, *J Am Chem Soc*, 2012, **134**, 7258-7261.
31. M. E. Snowden, M. Dayeh, N. A. Payne, S. Gervais, J. Mauzeroll and S. B. Schougaard, *Journal of Power Sources*, 2016, **325**, 682-689.
32. Y. Takahashi, A. Kumatani, H. Munakata, H. Inomata, K. Ito, K. Ino, H. Shiku, P. R. Unwin, Y. E. Korchev, K. Kanamura and T. Matsue, *Nat Commun*, 2014, **5**.
33. H. Inomata, Y. Takahashi, D. Takamatsu, A. Kumatani, H. Ida, H. Shiku and T. Matsue, *Chem Commun*, 2019, **55**, 545-548.
34. B. Tao, L. C. Yule, E. Daviddi, C. L. Bentley and P. R. Unwin, *Angewandte Chemie International Edition*, 2019, **58**, 4606-4611.
35. M. Dayeh, M. R. Z. Ghavidel, J. Mauzeroll and S. B. Schougaard, *Chemelectrochem*, 2019, **6**, 195-201.
36. D. Takamatsu, Y. Koyama, Y. Orikasa, S. Mori, T. Nakatsutsumi, T. Hirano, H. Tanida, H. Arai, Y. Uchimoto and Z. Ogumi, *J Electrochem Soc*, 2014, **161**, A1447-A1452.
37. C. Kim, N. S. Norberg, C. T. Alexander, R. Kostecki and J. Cabana, *Adv Funct Mater*, 2013, **23**, 1214-1222.
38. T. Ohzuku, A. Ueda and N. Yamamoto, *J Electrochem Soc*, 1995, **142**, 1431-1435.
39. D. Young, A. Ransil, R. Amin, Z. Li and Y. M. Chiang, *Adv Energy Mater*, 2013, **3**, 1125-1129.
40. D. M. Cunha, T. A. Hendriks, A. Vasileiadis, C. M. Vos, T. Verhallen, D. P. Singh, M. Wagemaker and M. Huijben, *ACS Applied Energy Materials*, 2019, **2**, 3410-3418.
41. M. G. Verde, L. Baggetto, N. Balke, G. M. Veith, J. K. Seo, Z. Y. Wang and Y. S. Meng, *Acs Nano*, 2016, **10**, 4312-4321.
42. Y. Takahashi, Y. Kobayashi, Z. Wang, Y. Ito, M. Ota, H. Ida, A. Kumatani, K. Miyazawa, T. Fujita, H. Shiku, Y. E. Korchev, Y. Miyata, T. Fukuma, M. Chen and T. Matsue, *Angewandte Chemie International Edition*, 2020, **59**, 3601-3608.
43. S. Shiraki, H. Oki, Y. Takagi, T. Suzuki, A. Kumatani, R. Shimizu, M. Haruta, T. Ohsawa, Y. Sato, Y. Ikuhara and T. Hitosugi, *J Power Sources*, 2014, **267**, 881-887.
44. K. Kataoka, Y. Takahashi, N. Kijima, H. Hayakawa, J. Akimoto and K.-i. Ohshima, *Solid State Ionics*, 2009, **180**, 631-635.
45. H. Xia, L. Lu and G. Ceder, *J Power Sources*, 2006, **159**, 1422-1427.
46. N. Elgrishi, K. J. Rountree, B. D. McCarthy, E. S. Rountree, T. T. Eisenhart and J. L. Dempsey, *J Chem Educ*, 2018, **95**, 197-206.
47. D. Y. W. Yu, C. Fietzek, W. Weydanz, K. Donoue, T. Inoue, H. Kurokawa and S. Fujitani, *J Electrochem Soc*, 2007, **154**, A253-A257.
48. Y. H. Rho and K. Kanamura, *Journal of Solid State Chemistry*, 2004, **177**, 2094-2100.